Journal of Power Sources xxx (2018) xxx-xxx

ELSEVIER

Contents lists available at ScienceDirect

Journal of Power Sources

journal homepage: www.elsevier.com

Self-assembled Mn_3O_4/C nanosphere as high-performance anode materials for lithium ion batteries

Kewei Liu[a, 1], Feng Zou[a, 1], Yuandong Sun[a], Zitian Yu[a], Xinye Liu[a], Leyao Zhou[a], Yanfeng Xia[a], Bryan D. Vogt[b], Yu Zhu[a, *]

[a] *Department of Polymer Science, University of Akron, Akron, OH 44325, United States*
[b] *Department of Polymer Engineering, University of Akron, Akron, OH 44325, United States*

ARTICLE INFO

Keywords:
Mn_3O_4
Self-assembly
Metal organic complex
Hierarchical structure
Lithium ion battery

ABSTRACT

A self-assembled Manganese (Mn) based metal organic complex (Mn-MOC) with spherical structure was synthesized via a solvothermal reaction. The Mn-MOC precursor materials were converted to hierarchical porous Mn_3O_4/C nanospheres through thermal annealing treatment. These nanospheres exhibited a high reversible specific capacity (1237 mAh/g at 200 mA/g), excellent ratability (425 mAh/g at 4 A/g), and extremely long cycle life (no significant capacity fading after 3000 cycles at 4A/g) as an anode in lithium ion batteries. The notable capability for lithium storage is attributed to the unique porous hierarchical structure of the Mn_3O_4/C nanospheres, which consisted of homogeneously distributed Mn_3O_4 nanocrystals with thin carbon shells. Such a desired nanostructure not only provided large reaction surface area and enhanced electrical conductivity, but also promoted the formation of stable solid electrolyte interphase (SEI) and accommodated the volume change of the conversion reaction type electrode.

1. Introduction

Lithium ion batteries (LIBs), as a crucial power source component in electronics and renewable energy generation systems, have been intensively explored in the past few decades [1,2]. The commercial anode for LIBs is based on graphite, which has a theoretical specific capacity of 372 mAh/g. The limited theoretical capacity of graphite cannot satisfy the emerging applications such as electrical and hybrid vehicles, where LIBs with significant higher energy density and power density are required [3]. Therefore, it is necessary to develop advanced anode materials with significantly larger reversible specific capacity [4,5]. Transition metal oxides (MO_x, where M is Mn, Co, Ni, Cu or Fe etc.) are promising anode candidate materials, owing to their high theoretical capacity and low cost [6,7]. Among those materials, Mn_3O_4 has been intensively investigated as one of the most promising anode materials due to its abundance, low oxidation potential and competitive electrochemical performance [7,8]. However, several issues hamper the utilization of transition metal oxides as anode materials in LIBs: First, the poor intrinsic electrical conductivity of metal oxides limits the electron transfer throughout the electrode, leading to poor active materials utilization and low ratability [9]. Second, the large volume expansion and shrinkage of the metal oxides during the lithiation and delithiation can result in electrode pulverization that promotes capacity fading during cycling [10]. It has been well recognized that the nano-engineering and carbon hybridization can be effective ways to overcome or limit these issues [11–16]. One such approach is through use of metal organic complex (MOC) derived carbon coated metal oxide, which exhibited improved electrical conductivity and good accommodation of the strain during the lithiation and delithiation process, as an emergent class of novel anode materials in LIBs [17–19]. For instance, mesoporous Fe_2O_3 that was derived from an iron-based metal organic frameworks (MOFs) [20] exhibited specific capacity of 911 mAh/g after 50 charge/discharge cycles. Similarly, MOFs are effective precursors for ZnO@ZnO quantum dots/C nanorods that were reported to deliver a reversible specific capacity of 699 mAh/g after 100 cycles [21]. NiO-CoO-C microspheres with a yolk-shell structure [22] exhibited a high specific capacity of 1194 mAh/g and good ratability (821 mAh/g at 2 A/g). Many additional MOC derived carbon coated metal oxide materials, including Co_3O_4, Co_3O_4/Co, CuO/Cu_2O and ZnO/$ZnFe_2O_4$ etc., have been explored and exhibited good lithium storage

---

[*] Corresponding author.
Email address: yu.zhu@uakron.edu (Y. Zhu)
[1] K. Liu and F. Zou contributed equally to this work.

https://doi.org/10.1016/j.jpowsour.2018.05.064
Received 21 January 2018; Received in revised form 17 April 2018; Accepted 17 May 2018
Available online xxx
0378-7753/

capability [23–27]. Despite these successes, due to the intrinsic volume change of the metal oxide anode during the cycling that can lead to pulverization of the anode, the extended cycle life (over 1000 cycles) of metal oxide anode has rarely been demonstrated and represents a challenge for the further development of this class of anode materials.

In this work, a facile method to synthesize highly porous Mn_3O_4/C nanospheres with hierarchical structure was achieved by self-assembly to form spherical Mn based MOC, followed by a facile thermal annealing process. The Mn_3O_4/C nanospheres consisted of homogeneously distributed Mn_3O_4 nanocrystals with conformal carbon coating. Such a hierarchical, porous structure provided both good electrical conductivity and volume changes accommodation capability, which were desired for transition metal oxide based conversion reaction type electrode [28,29]. These characteristics led to high specific capacity, excellent ratability and ultra-long cycle life in a lithium-ion half-cell for the Mn_3O_4/C nanosphere electrode.

2. Experimental

2.1. Materials and characterization

Manganese nitrate (50-52% aqueous solution, TREM CHEMICALS), trimesic acid (95% Sigma-Aldrich), ethanol (200 proof, Decon Laboratories, Inc.), N,N-dimethylformamide (DMF, ACS grade, EMD), N-methyl-2-pyrrolidone (NMP, 99.5% EMD), fluoroethylene carbonate (FEC, 98% Alfa Aesar), Super P carbon (MTI Corporation), and lithium foil (15.6 mm in diameter and 0.25 mm in thickness, MTI Corporation) were used as received. Poly(acrylic acid) (PAA, $M_w = 450000\,g\,mol^{-1}$) was purchased from Scientific Polymer Products, Inc.

The SEM and TEM images were collected using JEOL JSM-7401F and JEOL 1203 microscopes, respectively. HRTEM images, and corresponding EDX maps were taken by FEI Tecnai G2 F20 equipped with an EDAX SUTW (super ultrathin window) energy-dispersive X-ray spectrometer (EDAX). Powder XRD speactra were obtained by using a Rigaku Ultima IV X-ray diffractometer with a Cu Kα radiation ($\lambda = 1.5604$ Å). TGA were performed on a Q500 station (TA Instruments) under Ar or air with a ramp rate of 5 °C/min. The surface area was measured with a Micromeritics TriStar II instrument (Micromeritics VacPrep 061). The sample was degassed at 80 °C for 12 h, prior to determining specific surface area, Nitrogen adsorption/desorption isotherms were obtained at 77 K using a TriStar II (Micromeritics). The Brunauer-Emmett-Teller (BET) method was used to determine the specific surface area in the relative vapor pressure range of 0.04–0.27. The nitrogen adsorption isotherm was used to determine the pore size distribution using the Barrett-Joyner-Halenda (BJH) model. The cyclic voltammetry profile was obtained by using a CHI608E electrochemical workstation with a scan rate of 0.2 mV/s. Galvanostatic charge and discharge tests were carried out by using a Battery Analyzer BST-8A (MTI) within the voltage range of 0.005–3 V (*vs.* Li/Li$^+$).

2.2. Synthesis of Mn-MOC

The Mn-MOC was synthesized via a solvothermal reaction. 0.1 g (50-52% wt) $Mn(NO_3)_2$ aqueous solution, and 0.03 g trimesic acid were dissolved in a solution mixture of 10 ml DMF and 10 ml ethanol under vigorous stir and then transferred into a Teflon-lined autoclave. The autoclave was heated up to 150 °C and held at 150 °C for 6 h for the reaction. The solids were washed with ethanol four times. The as-prepared Mn-MOC was collected by centrifuging (4000 rpm) and drying (80 °C).

2.3. Synthesis of Mn_3O_4/C nanosphere

The as-prepared Mn-MOC was placed in a combustion boat and inserted into a tube furnace under argon atmosphere. Then the sample was heated up to 500 °C using a temperature ramp of 4 °C/min and held for 1 h. After the furnace was naturally cooled down to room temperature, the powder of Mn_3O_4/C nanosphere was collected.

2.4. Battery fabrication

The electrode slurry was prepared by mixing 70% active material, 15% Super P carbon, and 15% PAA with NMP. The slurry was cast on copper foil using a doctor blade and dried at 80 °C overnight. The electrode was punched into disks with a diameter of 5/16 inch. The mass loading of the active materials is 0.6 mg/cm^2. Lithium metal foil was used as counter electrode and 1 M lithium hexafluorophosphate in EC/DEC (1:1 v/v) with 10% fluoroethylene carbonate was used as the electrolyte. The coin cell was assembled in an argon filled glovebox with oxygen and water content below 0.5 ppm.

3. Results and discussion

The procedure to fabricate the highly porous hierarchical Mn_3O_4/C nanosphere is illustrated in Fig. 1. The porous spherical manganese metal organic complex (Mn-MOC) was first prepared via a hydrothermal reaction. The Mn-MOC was then annealed in Ar to transform the manganese ion into manganese oxide and decomposing the organic ligand and to form carbon layers. The resulting Mn_3O_4/C nanospheres exhibit a highly porous hierarchical structure.

To synthesize the Mn-MOC, a hydrothermal reaction was performed with manganese nitrate as the metal source and trimesic acid as the organic ligand. As shown in Fig. 2a, the as prepared Mn-MOC exhibited a uniform spherical structure with a diameter of ~400 nm (inset picture in Fig. 2a). It is worthwhile to note that no surfactant or other templat-

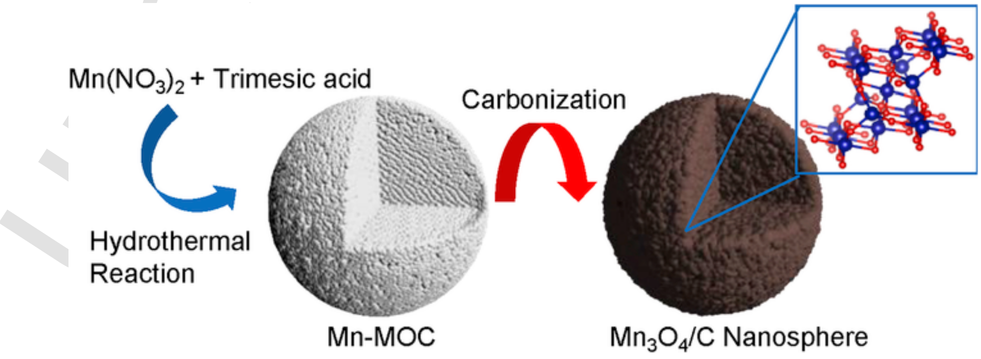

Fig. 1. Schematic illustration of the fabrication procedure for the Mn_3O_4/C nanospheres.

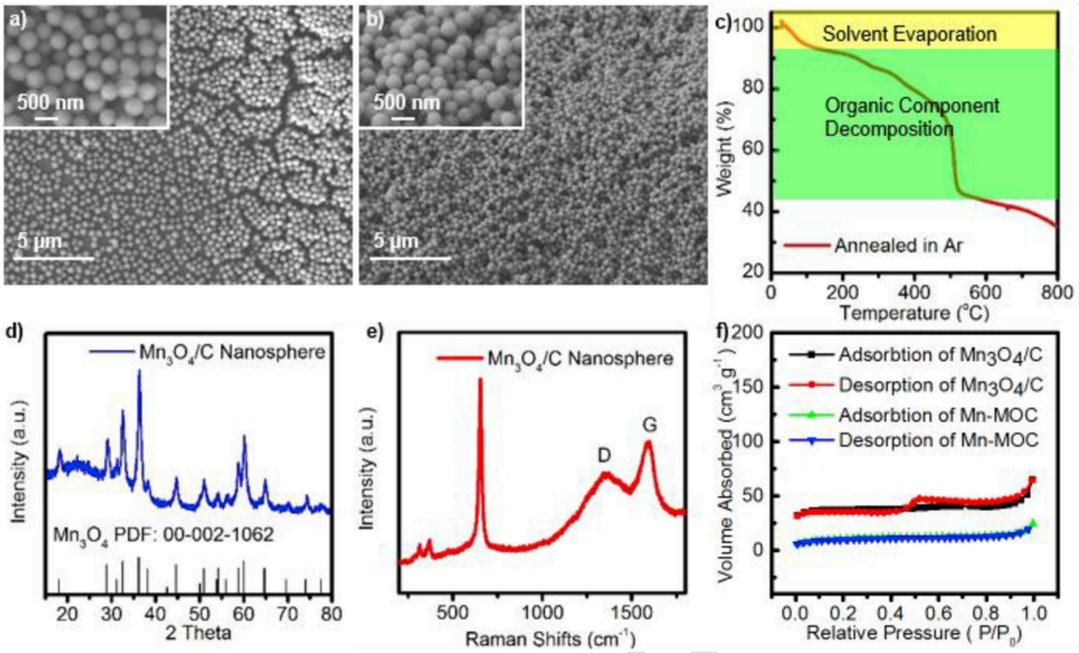

Fig. 2. a, b) SEM images of Mn-MOC and Mn_3O_4/C nanosphere after carbonization. The inset pictures were taken under higher magnifications. c) TGA analysis of the Mn-MOC annealed under Ar with a ramp rate of 5 °C/min from room temperature to 800 °C. d) XRD pattern of the as prepared Mn_3O_4/C nanospheres. Standard XRD pattern of Mn_3O_4 (PDF No. 00-002-1062) was shown for comparison. e) Raman spectrum of the Mn_3O_4/C nanosphere. f) The BET results of the Mn-MOC and Mn_3O_4/C nanosphere. The BET surface areas of Mn-MOC and Mn_3O_4/C nanosphere were determined to be $34.9\,m^2\,g^{-1}$ and $111.2\,m^2\,g^{-1}$, respectively.

ing materials were used to generate this uniform nanosphere structure, which renders this method highly scalable. After annealing under argon (Ar), the spherical structure was well-maintained (Fig. 2b). The carbonization temperature was determined to be 500 °C by TGA analysis (Fig. 2c). The weight loss below 150 °C could be attributed to the evaporation of solvent trapped in the pores of Mn-MOC nanospheres [30]. From 150 to 500 °C, an obvious weight loss was witnessed, corresponding to the decomposition of organic components and the formation of carbon coated manganese oxide [31]. The weight loss above 500 °C can be assigned to the reduction of manganese oxide to metallic manganese by carbothermal reaction [18]. Based on the TGA results, the Mn-MOC was annealed at 500 °C under Ar atmosphere to generate the carbon coated manganese oxide. The components in the final product was characterized by XRD. As depicted in Fig. 2d, all the diffraction peaks can be indexed to the standard Mn_3O_4 (PDF NO. 00-002-1062). Raman spectrum of the annealed product was also obtained, as shown in Fig. 2e, with the peaks at 315, 370, 655 cm^{-1} corresponding to Mn_3O_4 [32], which was consistent with XRD result. The peak at 1350, and 1590 cm^{-1}, which are characteristic D and G peaks for carbonaceous materials [33], were also clearly observed, which confirmed the existence of carbon in the Mn_3O_4/C nanosphere. The carbon content was measured to be ~28 wt% based on TGA analysis (Fig. S1). The pore texture was determined from the N_2 adsorption-desorption isotherms as shown in Fig. 2f. For Mn-MOC, the pore size distribution demonstrated that there was no dominate mesopore size and that the pore population appears to be greater for the micropores (Fig. S2). In this case, the pores in Mn-MOC were < 4 nm. In contrast, the pore size distribution of Mn_3O_4/C as shown in Fig. S2 exhibited a well defined mesopore size. The average pore size for Mn_3O_4/C nanosphere was 4.8 nm, indicating the formation of nanopores during Mn-MOC carbonization. The hysteresis loop in the adsorption-desorption isotherms for the Mn_3O_4/C nanosphere (Fig. 2f) is consistent with the presence of nanopores. Additionally, the specific surface area of Mn_3O_4/C nanospheres determined from the BET method was $111.2\,m^2/g$, while the original surface area of the Mn-MOC was estimated to only be $34.9\,m^2/g$ (Fig. 2f). The high surface area for the Mn_3O_4/C nanosphere is consistent with the formation of a highly porous structure that can improve reaction interfaces between electrolyte and active materials.

The high resolution TEM (HRTEM) images of Mn_3O_4/C nanosphere are shown in Fig. 3a and b. Compared with the TEM image of as prepared Mn-MOC (Fig. S3), the inset picture in Fig. 3a of the Mn_3O_4/C demonstrates a highly porous nanosphere with hierarchical structure. The ultrafine Mn_3O_4 nanocrystals can be clearly observed in Fig. 3a. The d-spacing of 2.75 Å and 3.09 Å can be indexed to the (103) and (112) interplane of Mn_3O_4, consistent with the XRD pattern of Mn_3O_4/C nanospheres. Fig. 3b illustrates the edge of the Mn_3O_4 nanocrystals in a Mn_3O_4/C nanosphere using HRTEM. A carbon layer with thickness of 3–5 nm is clearly visible. The Z-contrast image (Fig. 3c) collected in scanning TEM (STEM) mode clearly presents the highly porous hierarchical structure. The elemental mapping images of carbon, manganese and oxygen (Fig. 3d–f), were obtained via energy-dispersive X-ray spectroscopy (EDX) in STEM mode, which elucidated the homogeneous distribution of C, Mn and O, indicating the uniform Mn_3O_4/C nanospheres.

In order to investigate the lithium storage mechanism of the Mn_3O_4/C anode, cyclic voltammogram was obtained at a scan rate of 0.2 mV/s within the voltage range from 0.005 V to 3 V (vs. Li/Li^+) (Fig. 4a). A small cathodic peak from the first cycle observed at 0.31 V can be attributed to the decomposition of the electrolyte and formation of the SEI layer. A cathodic shoulder peak located at 1.0 V corresponds to the reduction of Mn_3O_4 to MnO and generation of Li_2O [34]. The main cathodic peak at 0.03 V was assigned to the reduction reaction of lithium ion with Mn_3O_4. In the anodic process, the peaks at 1.18 V and 2.1 V reveals the oxidation of metallic manganese to Mn^{2+} and a higher oxidation state of Mn^{3+} [35]. In the following cycles, the reduction peak shifted to a higher voltage of 0.28 V due to the structure changes resulted from lithiation in the first cycle [15,36]. All the scan curves are perfectly overlapped, demonstrating the excellent reversibility for lithium storage. The overall lithium storage mechanism of the

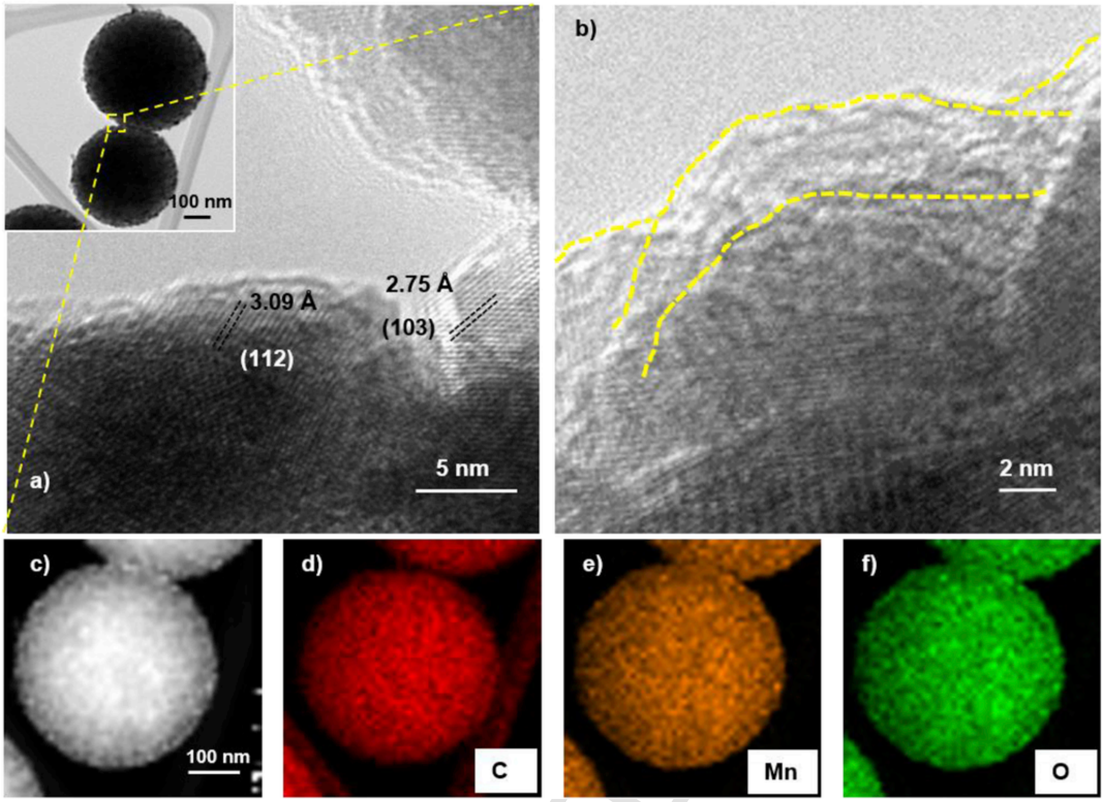

Fig. 3. a) HRTEM image was taken by focusing at the noted area in inset picture. The inset picture is the TEM image of highly porous hierarchical. The *d*-spacing was determined to be 2.75 Å and 3.09 Å, corresponding to the (103) and (112) planes. b) The HRTEM image of Mn_3O_4/C nanosphere focusing at interface of carbon layer and Mn_3O_4 nanocrystal. The carbon layer was indicated as the area between yellow dash lines c) STEM Z-contrast image and the corresponding elemental EDX mapping images of (d) carbon, (e) manganese, and (f) oxygen. C, Mn and O were homogeneously distributed, indicating the well self-assembly of nano-sized Mn_3O_4 with carbon coating in the spherical structure. (For interpretation of the references to colour in this figure legend, the reader is referred to the Web version of this article.)

Mn_3O_4 nanosphere anode can be described by the equation below [37]:

$$Mn_3O_4 + 8Li^+ + 8e^- \leftrightarrow 3Mn + 4Li_2O \quad (1)$$

The Galvanostatic charge/discharge profiles at a current density of 200 mA/g was shown in Fig. 4b. A plateau observed at around 0.4 to 0.25 V (vs. Li/Li^+) in the first discharge corresponds to the SEI formation and reduction reaction of manganese oxide, in accordance with the CV test. The first discharge and charge capacity reached high up to 2022 mAh/g and 1288 mAh/g, respectively. The irreversible capacity could be attributed to the consumption of lithium ions during the SEI film formation.

During the cyclability test at 200 mA/g (Fig. 4c), the capacity increased from 1242 mAh/g gradually to 1288 mAh/g after 190 cycles. The gradual increasing capacity during cycling is a common phenomenon for metal oxide based conversion electrode in LIBs, which can be associated with the amorphization of crystalline Mn_3O_4, promoting the lithium conversion kinetics and supplying more active sites for lithium storage [38,39]. In order to investigate the structural stability of the Mn_3O_4/C nanospheres, the cell was disassembled after the cycle test and the electrode was removed for TEM characterization. The TEM image of the Mn_3O_4/C nanosphere after long cycles (Fig. S4) demonstrates that the highly porous spherical structure was quite robust and stable during the oxidation and reduction reactions.

The *in-situ* generated carbon layer also improved the conductivity of the Mn_3O_4 nanospheres. To validate this, the Mn_3O_4 nanospheres without carbon film were prepared by annealing the Mn_3O_4/C sample in air at 300 °C for 2h with a ramp rate of 5 °C/min. During this process, the carbon shell was removed by oxidation. The resulting pure Mn_3O_4 nanospheres were used to build half-cells with lithium metal as counter electrode. The electrochemical impedance spectra (EIS) of Mn_3O_4/C and pure Mn_3O_4 half cells were collected in Fig. S5. As shown in Fig. S5, a much smaller internal charge transfer resistance was observed in Mn_3O_4/C as compared with pure Mn_3O_4 without carbon shell, indicating a faster electron transfer in Mn_3O_4/C sample. In addition, a steeper low-frequency tail in Mn_3O_4/C nanosphere indicated a higher Li ion conductivity, promoting the Li uptake and extraction kinetics [39].

The rate capability of the Mn_3O_4/C nanosphere as anode in LIBs was evaluated at current densities from 200 mA/g to 4 A/g. The electrode delivered an average capacity of 1237 mAh/g, 1030 mAh/g, 680 mAh/g, 425 mAh/g at 200 mA/g, 500 mA/g, 1 A/g, 2 A/g, and 4 A/g, respectively, demonstrating excellent lithium ion and electron mobility. Note that when the current density was returned to 200 mA/g, the capacity recovered to 1351 mAh/g, confirming the good reversibility of the Mn_3O_4/C anode. To further investigate the stability of the Mn_3O_4/C nanosphere as anode material, a 3000-cycle test was carried out at a high current density of 4 A/g. A current density of 200 mA/g was performed in the first three cycles to form stable SEI layers. An initial specific capacity of 448 mAh/g could be delivered when the current density increased to 4 A/g. After 3000 cycles, the electrode still maintained a specific capacity of 508 mAh/g, presenting an extraordinary stability. To the best of our knowledge, this is the best cycle performance ever reported for a Mn_3O_4 based anode in LIBs. The comparison to other works is presented in Table S1.

The promising Li storage capability of the Mn_3O_4/C nanosphere could be assigned to the following unique properties: 1) the ultrafine Mn_3O_4 nanocrylstal could enhance the kinetics for the lithium storage, shorten the diffusion path for lithium ions. 2) uniform carbon coating enabled the formation of stable SEI layer. It also enhanced the conduc-

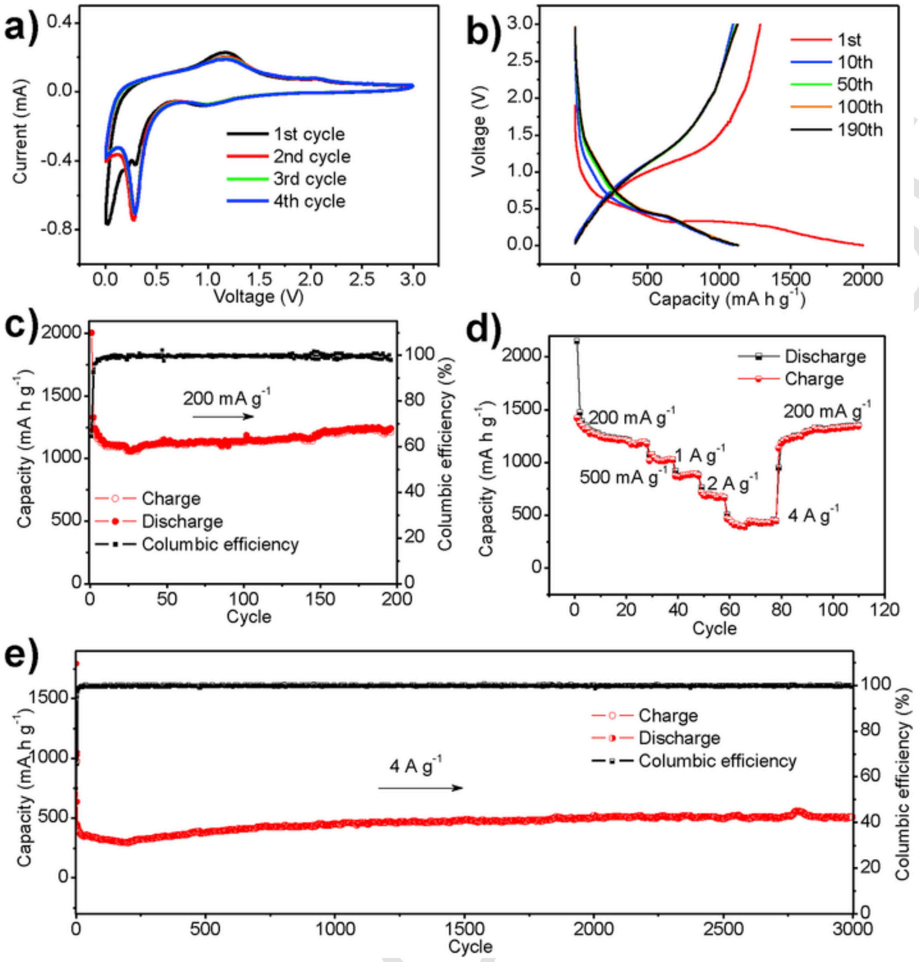

Fig. 4. Electrochemical performance of Mn_3O_4/C nanosphere as anode in LIBs. a) Cyclic voltammogram of Mn_3O_4/C nanosphere performed at a scan rate of 0.2 mV/s within the voltage range of 0.005–3 V (vs. Li/Li^+). b) Galvanostatic charge and discharge profiles for the 1st, 10th, 50th, 100th, 190th cycles at a current density of 200 mA/g (Voltage vs. Li/Li^+). c) Cycle performance at a current density of 200 mA/g d) Specific capacities at current densities of 200 mA/g, 500 mA/g, 1 A/g, 2 A/g and 4 A/g. e) Long cyclability test at a current density of 4 A/g.

tivity that facilitated the charge transfer during operation. 3) the highly porous structure provided a high surface area which is beneficial for the efficient contact between electrode material and the electrolyte. It could effectively accomodatet the volume change during the cylclying, maintain the morphology of the electrode materials. In this regard, a Mn_3O_4/C nanosphere with hierarchical structure was endowed with high reversible capacity, excellent stability and ratability as LIB anode.

4. Conclusion

In summary, a scalable method was explored to synthesize a highly porous hierarchical Mn_3O_4/C nanospheres from a self-assembled Mn-MOC. The porous hierarchical Mn_3O_4/C nanospheres consisted of nanocrystal Mn_3O_4 particles with uniform thin carbon shells. The unique porous structure provided a large active surface area for electrolyte contact. Meanwhile, the carbon shell on Mn_3O_4 nanocrystal significantly enhanced the electrical conductivity, leading to the formation of stable and robust SEI layers. The porous hierarchical Mn_3O_4/C nanospheres aslo accommodated the volume changes during the cycling, maintaining the morphology of electrode materials. The lithium-ion battery with Mn_3O_4/C nanosphere anode exhibited a high reversible specific capacity of 1237 mAh/g, excellent ratability of 425 mAh/g at 4 A/g, and extremely long cycle life (no significant capacity fading after 3000 cycles at 4 A/g).

Acknowledgements

The authors thank Dr. B. Wang for the help with the SEM, Dr. M. Gao for the help of HRTEM and E. Laughlin for technical support. The TEM observations using FEI Tecnai F20 were carried out at the Liquid Crystal Institute Characterization Facility of Kent State University. The authors thank the financial support from the National Science Foundation (NSF) through NSF-CBET 1505943, 1706681, NSF-DMR 1554851 and Ohio Federal Network Research (OFRN) of through the Center of Excellence.

Appendix A. Supplementary data

Supplementary data related to this article can be found at https://doi.org/10.1016/j.jpowsour.2018.05.064.

References

[1] B. Dunn, H. Kamath, J.-M. Tarascon, Science 334 (2011) 928–935.
[2] K.T. Nam, D.-W. Kim, P.J. Yoo, C.-Y. Chiang, N. Meethong, P.T. Hammond, Y.-M. Chiang, A.M. Belcher, Science 312 (2006) 885–888.
[3] J.M. Tarascon, M. Armand, Nature 414 (2001) 359–367.
[4] J. Wang, G. Zhang, Z. Liu, H. Li, Y. Liu, Z. Wang, X. Li, K. Shih, L. Mai, Nanomater. Energy 44 (2018) 272–278.
[5] T. Li, X. Li, Z. Wang, H. Guo, J. Power Sources 342 (2017) 495–503.

[6] P. Poizot, S. Laruelle, S. Grugeon, L. Dupont, J.M. Tarascon, Nature 407 (2000) 496–499.
[7] M.V. Reddy, T. Yu, C.H. Sow, Z.X. Shen, C.T. Lim, G.V. Subba Rao, B.V.R. Chowdari, Adv. Funct. Mater. 17 (2007) 2792–2799.
[8] F.M. Courtel, Y. Abu-Lebdeh, I.J. Davidson, Electrochim. Acta 71 (2012) 123–127.
[9] J. Jiang, Y. Li, J. Liu, X. Huang, C. Yuan, X.W. Lou, Adv. Mater. 24 (2012) 5166–5180.
[10] M.V. Reddy, G.V. Subba Rao, B.V.R. Chowdari, Chem. Rev. 113 (2013) 5364–5457.
[11] P.-C. Chen, G. Shen, Y. Shi, H. Chen, C. Zhou, ACS Nano 4 (2010) 4403–4411.
[12] Z. Wang, D. Luan, S. Madhavi, Y. Hu, X.W. Lou, Energy Environ. Sci. 5 (2012) 5252–5256.
[13] L. Li, Z. Guo, A. Du, H. Liu, J. Mater. Chem. 22 (2012) 3600–3605.
[14] Z. Wang, D. Luan, S. Madhavi, Y. Hu, X.W. Lou, Energy Environ. Sci. 5 (2012) 5252–5256.
[15] S.-K. Park, A. Jin, S.-H. Yu, J. Ha, B. Jang, S. Bong, S. Woo, Y.-E. Sung, Y. Piao, Electrochim. Acta 120 (2014) 452–459.
[16] Z.-S. Wu, W. Ren, L. Wen, L. Gao, J. Zhao, Z. Chen, G. Zhou, F. Li, H.-M. Cheng, ACS Nano 4 (2010) 3187–3194.
[17] G. Zhang, B.Y. Xia, C. Xiao, L. Yu, X. Wang, Y. Xie, X.W. Lou, Angew. Chem. Int. Ed. 125 (2013) 8805–8809.
[18] F. Zou, Y.-M. Chen, K. Liu, Z. Yu, W. Liang, S.M. Bhaway, M. Gao, Y. Zhu, ACS Nano 10 (2016) 377–386.
[19] L. Zhang, H.B. Wu, S. Madhavi, H.H. Hng, X.W. Lou, J. Am. Chem. Soc. 134 (2012) 17388–17391.
[20] X. Xu, R. Cao, S. Jeong, J. Cho, Nano Lett. 12 (2012) 4988–4991.
[21] G. Zhang, S. Hou, H. Zhang, W. Zeng, F. Yan, C.C. Li, H. Duan, Adv. Mater. 27 (2015) 2400–2405.
[22] J. Leng, Z. Wang, X. Li, H. Guo, H. Li, K. Shih, G. Yan, J. Wang, J. Mater. Chem. 5 (2017) 14996–15001.
[23] L. Hu, N. Yan, Q. Chen, P. Zhang, H. Zhong, X. Zheng, Y. Li, X. Hu, Chem. Eur J. 18 (2012) 8971–8977.
[24] L. Hu, Y. Huang, F. Zhang, Q. Chen, Nanoscale 5 (2013) 4186–4190.
[25] F. Zou, X. Hu, Z. Li, L. Qie, C. Hu, R. Zeng, Y. Jiang, Y. Huang, Adv. Mater. 26 (2014) 6622–6628.
[26] Z. Yan, Q. Hu, G. Yan, H. Li, K. Shih, Z. Yang, X. Li, Z. Wang, J. Wang, Chem. Eng. J. 321 (2017) 495–501.
[27] T. Li, X. Li, Z. Wang, H. Guo, Y. Li, J. Wang, J. Mater. Chem. 5 (2017) 13469–13474.
[28] L. Ji, Z. Lin, M. Alcoutlabi, X. Zhang, Energy Environ. Sci. 4 (2011) 2682–2699.
[29] P.G. Bruce, B. Scrosati, J.-M. Tarascon, Angew. Chem. Int. Ed. 47 (2008) 2930–2946.
[30] A. Banerjee, R. Gokhale, S. Bhatnagar, J. Jog, M. Bhardwaj, B. Lefez, B. Hannoyer, S. Ogale, J. Mater. Chem. 22 (2012) 19694–19699.
[31] R. Wu, X. Qian, F. Yu, H. Liu, K. Zhou, J. Wei, Y. Huang, J. Mater. Chem. 1 (2013) 11126–11129.
[32] L. Malavasi, P. Galinetto, M.C. Mozzati, C.B. Azzoni, G. Flor, Phys. Chem. Chem. Phys. 4 (2002) 3876–3880.
[33] K. Liu, Y.-M. Chen, G.M. Policastro, M.L. Becker, Y. Zhu, ACS Nano 9 (2015) 6041–6049.
[34] T. Li, C. Guo, B. Sun, T. Li, Y. Li, L. Hou, Y. Wei, J. Mater. Chem. 3 (2015) 7248–7254.
[35] R. Wang, P. Liu, J. Lang, L. Zhang, X. Yan, Energy Storage Mater. 6 (2017) 53–60.
[36] G. Jian, Y. Xu, L.-C. Lai, C. Wang, M.R. Zachariah, J. Mater. Chem. 2 (2014) 4627–4632.
[37] N. Lavoie, P.R.L. Malenfant, F.M. Courtel, Y. Abu-Lebdeh, I.J. Davidson, J. Power Sources 213 (2012) 249–254.
[38] C. Peng, B. Chen, Y. Qin, S. Yang, C. Li, Y. Zuo, S. Liu, J. Yang, ACS Nano 6 (2012) 1074–1081.
[39] G. Zhou, D.-W. Wang, L.-C. Yin, N. Li, F. Li, H.-M. Cheng, ACS Nano 6 (2012) 3214–3223.